ChemBioChem

Research Article
doi.org/10.1002/cbic.202400311

Chemistry Europe
European Chemical Societies Publishing

www.chembiochem.org

OsO_2 as the Contrast-Generating Chemical Species of Osmium-Stained Biological Tissues in Electron Microscopy

Ruiyu Li,[a, b] Gregg Wildenberg,[c, d] Kevin Boergens,[e] Yingjie Yang,[e] Kassandra Weber,[e] Janek Rieger,[b] Ashley Arcidiacono,[b] Robert Klie,[e] Narayanan Kasthuri,*[c, d] and Sarah B. King*[a, b]

Electron imaging of biological samples stained with heavy metals has enabled visualization of subcellular structures critical in chemical-, structural-, and neuro-biology. In particular, osmium tetroxide (OsO_4) has been widely adopted for selective lipid imaging. Despite the ubiquity of its use, the osmium speciation in lipid membranes and the process for contrast generation in electron microscopy (EM) have continued to be open questions, limiting efforts to improve staining protocols and therefore high-resolution nanoscale imaging of biological samples. Following our recent success using photoemission electron microscopy (PEEM) to image mouse brain tissues with synaptic resolution, we have used PEEM to determine the nanoscale electronic structure of Os-stained biological samples. Os(IV), in the form of OsO_2, generates nanoaggregates in lipid membranes, leading to a strong spatial variation in the electronic structure and electron density of states. OsO_2 has a metallic electronic structure that drastically increases the electron density of states near the Fermi level. Depositing metallic OsO_2 in lipid membranes allows for strongly enhanced EM signals and conductivity of biological materials. The identification of the chemical species and understanding of the membrane contrast mechanism of Os-stained biological specimens provides a new opportunity for the development of staining protocols for high-resolution, high-contrast EM imaging.

Introduction

Osmium tetroxide (OsO_4) has been extensively used for enhancing membrane contrast in electron microscopy (EM) for the last several decades due to its lipid-selective chemical reactivity.[1–8] Conventional understanding of the mechanism of Os contrast generally focuses on the identity of Os as a "heavy metal", with a high atomic number.[9] However, the oxidation state and bonding of osmium in lipid membranes, and the reactions occurring during the staining process are surprisingly unknown. This has left puzzling questions for the broad community that uses OsO_4 chemistry for electron microscopy, such as why osmium staining improves the conductivity of biological samples and facilitates EM imaging without severe charging problems. The question of the chemical identity and formation mechanism of osmium compounds in lipid membranes has also hampered efforts to modify staining protocols of biological materials for EM to improve chemical uptake in large tissue samples, improve image contrast, or develop chemistries that don't require highly toxic osmium tetroxide. Reaction development has relied on exhaustive search rather than rational design.

Historically, the biological literature suggested that osmate esters are formed in the tails of unsaturated fatty acids in lipid membranes, as facilitated by the well-understood reaction of OsO_4 with alkenes.[10] The Os nuclei of the osmate esters present in regions with high lipid concentrations were suggested to be the source of improved electron scattering in SEM and TEM.[1] More recently, research on improving the staining of whole brain samples hypothesized the osmium species responsible for EM contrast is osmium(IV) (OsO_2), rather than the previously proposed osmium(VIII). Upon staining, the biological material underwent an observable color change in an *ex situ* model experiment, suggestive of the formation of Os(IV).[4] However, the presence of OsO_2 was not confirmed, and it was unclear how OsO_2 would impact the SEM contrast. X-ray photoelectron spectroscopy (XPS) of stained specimens showed the presence of a mixture of low Os oxidation states, but lacked the spatial resolution needed to determine the locations of different Os oxidation states.[11] Therefore, it is of vital importance to

[a] R. Li, S. B. King
Department of Chemistry, University of Chicago,
Chicago, IL, USA
E-mail: sbking@uchicago.edu

[b] R. Li, J. Rieger, A. Arcidiacono, S. B. King
James Franck Institute, University of Chicago,
Chicago, IL, USA

[c] G. Wildenberg, N. Kasthuri
Department of Neurobiology, The University of Chicago,
Chicago, IL, USA
E-mail: bobbykasthuri@uchicago.edu

[d] G. Wildenberg, N. Kasthuri
Argonne National Laboratory, Biosciences Division,
Lemont, IL, USA

[e] K. Boergens, Y. Yang, K. Weber, R. Klie
Department of Physics, University of Illinois Chicago,
Chicago, IL, USA

Supporting information for this article is available on the WWW under https://doi.org/10.1002/cbic.202400311

determine the local electronic structure of Os-stained biological materials on the nanoscale and unravel the reaction scheme of the osmium staining process.

We have recently demonstrated wide-field imaging of ultra-thin brain slices (UTBS) stained with OsO_4 and $K_4Fe(CN)_6$ with synaptic resolution using photoemission electron microscopy (PEEM).[12] PEEM is based on the photoelectric effect where a photon with energy greater than the work function of a material causes the emission of electrons with a spatial distribution that is magnified and mapped to a detector via electron lenses, as shown in Figure 1(a). PEEM probes the local electronic structure of imaged materials and has illustrated the potential for detailed surface mapping of biological materials at a submicrometer resolution.[13–17] Therefore, this technique facilitates identification of the electronic structure of osmium compounds used in biological staining, shedding light on how and why osmium staining improves sample conductivity and image contrast in electron microscopy.

In this paper, we show that biological materials stained with OsO_4 and $K_4Fe(CN)_6$ form OsO_2 nanoaggregates in the lipid membranes. OsO_2 behaves like a metal, possessing a high electron density of states (DOS) that crosses the Fermi level, and provides the needed conductivity and electron DOS for successful PEEM imaging of biological tissues. We propose a full mechanistic picture leading to OsO_2 formation, discuss possibilities for a likely slow step, and pinpoint specific routes for contrast improvement. As the speciation of osmium also plays an important role in the contrast and conductivity of samples for SEM and TEM that share the same staining protocol, the mechanism of Os staining and image contrast described here is equally critical for improving image quality of biological materials in the broader EM field.

Results and Discussion

Energy-Resolved PEEM Imaging

Figure 1(b) shows a PEEM image of a UTBS on a Au/*n*-SiO_2/Si substrate. Photoelectrons are emitted from the UTBS via a one-photon photoemission process using a broadband Hg arc lamp that generates ultra-violet (UV) photons. Brighter regions of Figure 1(b) indicate more photoemissive components whereas darker regions are biomaterials that have low photoemission yield. Based on comparison to SEM images of similar samples, the bright outlines depict neuron or organelle membranes that selectively bind osmium. The darker background consists of unstained regions of biological tissues, such as cytoplasm, that do not contain lipid bilayers. More specifically, the inset of Figure 1(b) is the zoom-in of the red box. The shaded region is the cross-section of a neural dendrite, and the bright solid spot within the cytoplasm is a mitochondrion. The difference in signal intensities allows us to visually distinguish the ultra-structure of biological material with subcellular resolution, and the features are comparable to what has been previously collected using SEM.[18]

The contrast observed in PEEM is due to stained and non-stained regions generating different intensities of photoelectrons. To understand why photoemission intensity varies spatially in the brain tissue, we performed energy-resolved PEEM to measure the local electronic structure of the UTBS. We used a high-pass energy filter to incrementally cut out photoelectrons with kinetic energy lower than an energy threshold and obtained a series of PEEM images at the same sample position. The photoemission intensity of an ROI is extracted as a function of photoelectron energy with respect to the Fermi level of the analyzer ($E-E_F$), and we compute the energy distribution of the photoelectrons by performing a numerical

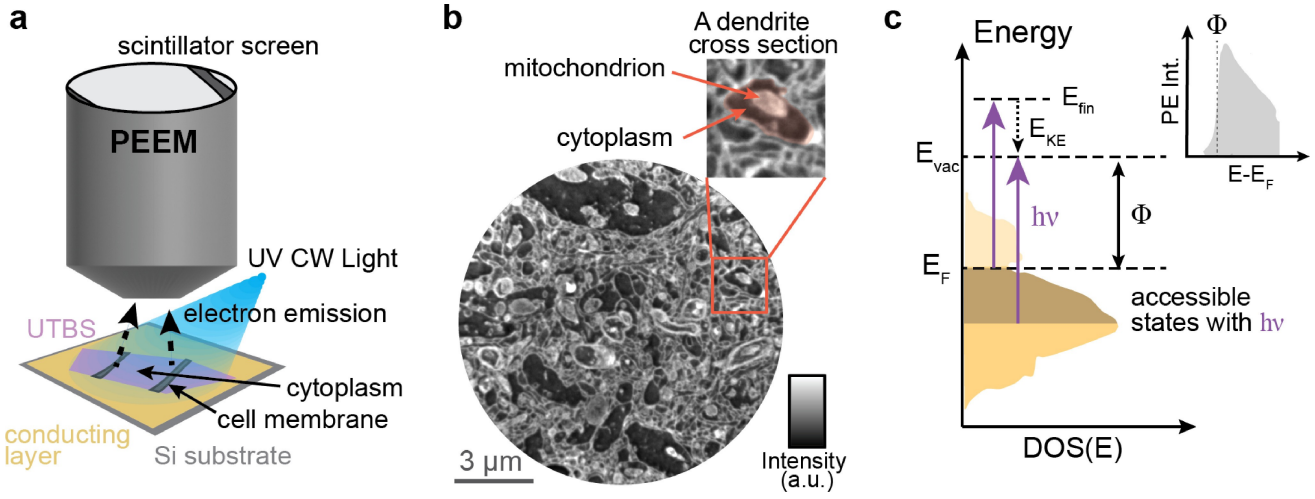

Figure 1. (a) A schematic of PEEM. An ultra-thin brain slice (UTBS) is placed on a gold-coated Si substrate, illuminated by a Hg lamp ultra-violet (UV) continuous-wave (CW) light source. (b) A representative PEEM image of mouse brain tissue. The bright contours indicate the cell membranes stained with osmium, and the dark features are the unstained cytoplasm. Ultrastructure can be clearly revealed, such as the neural dendrite and the mitochondrion in the shaded area in the inset. (c) Energy diagram of photoemission process, where electrons in occupied states below the Fermi level (E_F) are photoexcited with UV light of photon energy $h\nu$ to final states (E_{fin}) above the vacuum level (E_{vac}) with kinetic energy E_{KE}. The work function, Φ, is the energy difference between E_F and E_{vac}. The inset shows a schematic of the obtained photoemission spectrum from the accessible density of states (DOS) as a function of the kinetic energy of photoelectrons.

differentiation of the energy-resolved images (see Supporting Information, Energy-dependent PEEM imaging, for details). The low energy edge of this distribution, termed the secondary edge in the photoemission spectroscopy literature, can be used to determine the work function (Φ) of the material.[19,20] This value is the energy difference between the vacuum level and the Fermi level ($\Phi = E_{vac} - E_F$), as depicted in the energy diagram in Figure 1(c).

Figure 2(a, inset) shows three ROIs of varying signal intensities and their corresponding photoemission spectra. All three curves have been normalized to the peak intensities and offset vertically for clarity. Despite variation in the total photoemission counts, the three ROIs display almost identical photoemission spectra. We estimated the relative values of the work function ($\Delta\Phi$) of each region by shifting the energy axis with respect to the secondary edge of the top spectrum ($\Delta(E - E_F)$). The relative work function was found by fitting each photoemission spectrum with an exponentially modified Gaussian function and looking for the energy cutoff corresponding to half of the maximum magnitude (see more details on data processing in the Supporting Information, Fitting of photoemission spectra). The dashed line in Figure 2(a) marks the secondary edges of the three spectra. As $\Delta\Phi_{bright} = 0$, the relative work functions for the gray and dark regions are 0.011 eV and 0.0213 eV, respectively, which are smaller than $\pm$0.05 eV (instrument resolution). This result indicates that there is no measurable work function variation across the sample even with the existence of heavy metal stains. Therefore, the image contrast that is observed with UTBS in PEEM cannot be due to sample work function variation, but must be due to a variation in the sample electronic structure.

The high energy sides of the photoemission spectra in Figure 2(a) are virtually identical within the energy resolution. No additional peaks can be identified in the spectra from the bright ROI, which would indicate distinctive electronic states in this region. The similarity in spectra makes it unlikely that there is a difference in contrast-generating chemical species across the sample. It is instead more likely that there exists a concentration gradient of a singular chemical species, resulting in variation in photoemission intensities as a function of space. As shown schematically in Figure 2(b), biological tissues, such as unstained cytoplasm, are typically considered to be insulating materials. For example, proteins commonly have optical absorption around 4.43 eV (280 nm),[21] and have a high ionization energy.[22] Therefore, the photon source used in this work can not photoemit efficiently from the occupied electronic states of pure biological tissues, resulting in low photoemission intensities. Similarly OsO_4 and Os(VIII) compounds are also insulators with large HOMO–LUMO gaps of 3.52 eV ($\approx$352 nm)[23] and large ionization potentials,[24] resulting in low photoemission yield. However, OsO_2 is known to have metallic properties,[25–27] providing OsO_2 with the requisite electronic structure for high photoemission yield.

Elemental Characterizations of Osmium Species

Similar to its well-studied Group 8 analog RuO_2, OsO_2 tends to form metal oxide aggregates.[25,27,28] Figure 3(a) shows a high-angle annular dark-field transmission electron microscopy (HAADF-STEM) image of UTBS on a TEM grid, where the bright contrast corresponds to atomic columns containing elements with high atomic numbers. Bright contrast in the HAADF image shows aggregates clustering along cell membranes. Energy dispersive spectroscopy (EDS) mapping of the same ROI (Figure 3(b)) shows that the bright aggregates are osmium-rich, confirming that osmium has indeed been deposited specifically in the lipid membranes. Figure 3(c) shows the corresponding

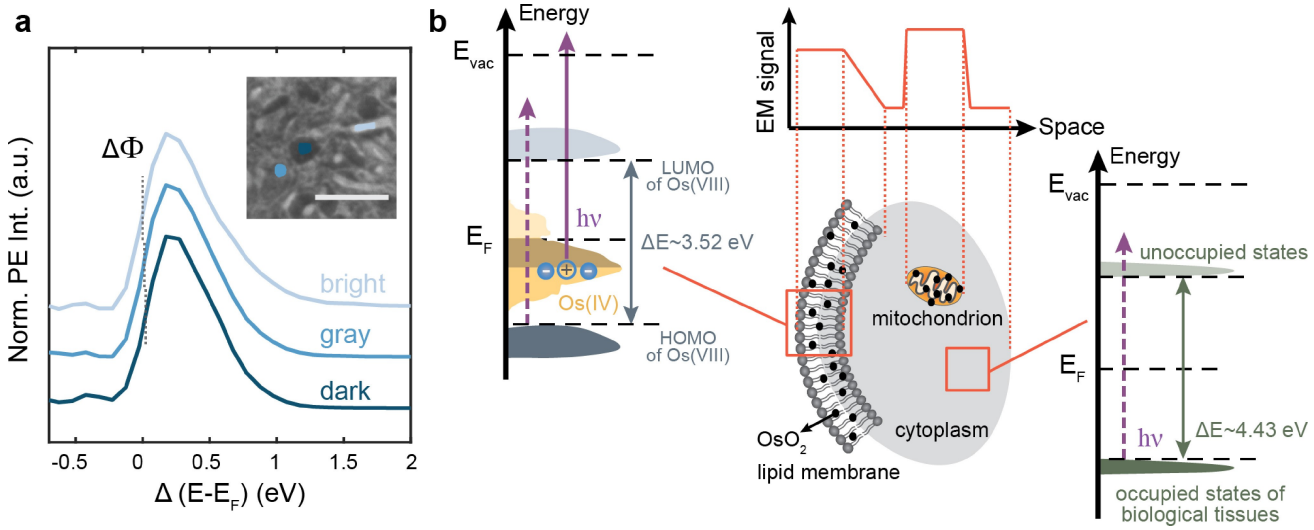

Figure 2. (a) Photoemission spectra of bright, gray and dark ROIs (corresponding different blue shades) shown in the inset. Dashed lines indicate work function relative to the secondary edge of the top spectrum (corresponds to the brightest region). The scale bar is 2 μm. (b) Energy diagrams comparing electron densities of osmium(IV) near the Fermi level with HOMO-LUMO gaps of Os(VIII) and biological tissues. Lipid membranes of cells and organelles such as mitochondria efficiently bind to osmium, generating stronger signals in EM images, whereas unstained regions such as cytoplasm generally yield low EM intensity.

Research Article
doi.org/10.1002/cbic.202400311
Chemistry Europe
European Chemical Societies Publishing

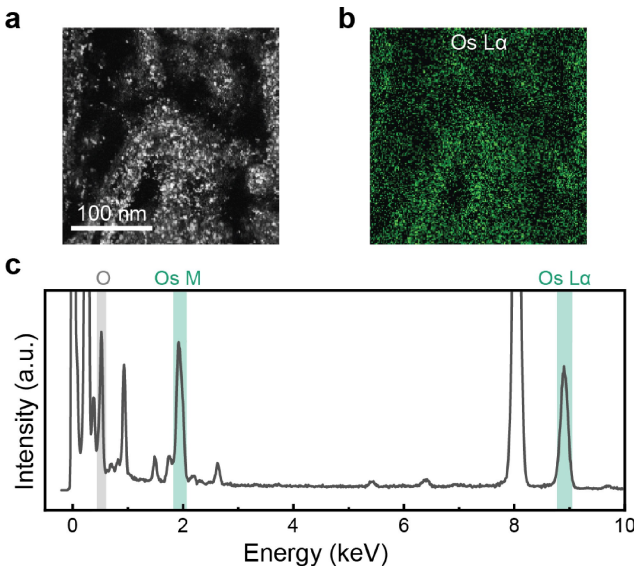

Figure 3. (a) A high-angle annular dark-field transmission electron microscopy (HAADF-STEM) image of an area with clear contrast of aggregates along cell membranes. (b) Energy dispersive spectroscopy (EDS) map from the Os Lα signal of the mapped area. (c) EDS spectrum of the elements detected, where the grey band highlights the O K signal at 0.525 keV, and green bands highlight Os M and Lα peaks at 1.91 keV and 8.91 keV, respectively. Note that other elements were also detected in the spectrum, but were disregarded for the purpose of the analysis.

EDS spectrum. Characteristic peaks of osmium M and Lα lines at 1.91 keV and 8.91 keV, respectively, can be clearly observed, and oxygen Kα signal is also confirmed at 0.53 keV. The average elemental ratio of Os:O from the Os-rich areas is calculated to be between 1:2 to 1:3, corroborating OsO_2 as the main osmium species. It is important to note that O signal is also detected in background areas where there is limited contrast from the bright clusters, indicating the likely overestimation of O composition in Os–O compounds. Furthermore, electron energy loss spectroscopy (EELS) was used to additionally verify the existence of both Os and O (see more discussion in the Supporting Information, EELS measurements). The combination of the EDS and EELS results indicates that Os most likely takes the valence state of IV, despite that some mixture of higher and lower states of osmium persists.[11,29]

Chemical Reactions for OsO_2 Formation

Hua *et al.* studied the formation of OsO_2 in tissue stains using color comparisons in a test tube experiment. From this result, they proposed a simple reaction scheme that invited future experiments to support the contributions of low-oxidation state osmium in EM staining.[4] Here, having confirmed OsO_2 and Os(IV) compounds as primary chemical species that provide PEEM contrast, we aim to deliver a more detailed and accessible description of the staining mechanism.

Buffered OsO_4 is introduced to biological tissue in its ionic water-soluble form, $[OsO_4(OH)_2]^{2-}$, see Step 1 in Figure 4. To ensure homogeneous staining across 100s μm-thick tissue block, osmium compounds passively diffuse through various layers of membranes to penetrate cells and organelles. This process is facilitated by $[OsO_4(OH)_2]^{2-}$ switching back and forth with its non-polar lipophilic form OsO_4.[30,31] In this reaction, Os(VIII) loses or gains two hydroxyl groups at the membrane-cytoplasm interface, resulting in an even distribution of Os(VIII) in the cell lipid phase.

In the next step (Step 2), OsO_4 selectively couples to specific sites in the lipid membranes to form bound osmium. It is widely

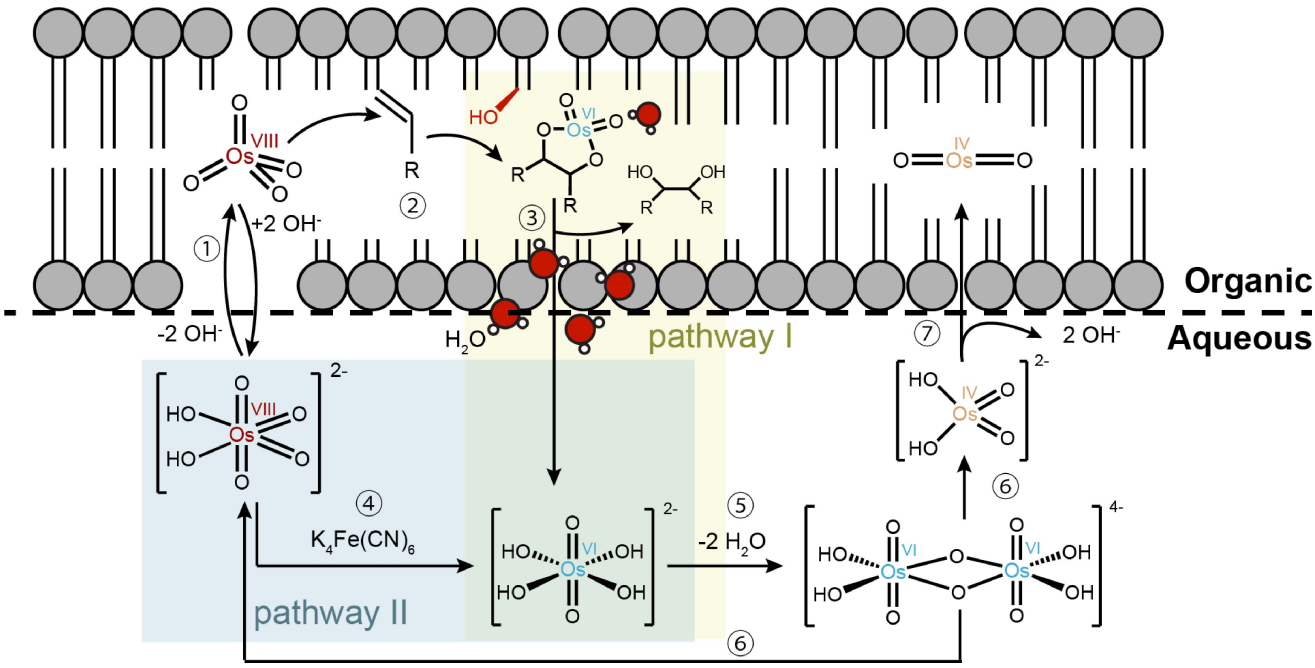

Figure 4. Schematic illustration of the formation and deposition of O_3O_2 in the lipid membrane during the staining process.

accepted that this process is realized via Sharpless dehydroxylation, where C=C bonds in unsaturated fatty acids attack an electropositive osmium center of the Os=O, resulting in the formation of an intermediate cyclic osmate ester (Os(VI)).[11,29,32] This ultimately leads to the reduction of Os(VIII) to Os(VI), as verified previously by XPS measurements.[11]

The transiently generated Os(VI) in Step 2 can be accessed through two different pathways, either via the migration of the osmate ester to the hydrophilic head of the lipids for spontaneous hydroxylation (Pathway I in Figure 4), or via reduction, initiated by additive $K_4Fe(CN)_6$, producing water-soluble $[OsO_2(OH)_4]^{2-}$ in the aqueous phase (Pathway II). In Pathway I, nearby water molecules or hydroxyl groups are necessary to promote hydroxylation (Step 3), but their origin in the lipid phase has not been well discussed in the literature. It is known that water can passively diffuse across lipid membranes to allow for osmotic equilibrium; this small population of water may serve as a potential –OH source in the membrane.[33] Additionally, it has been observed that osmium can migrate towards the membrane-water interface, resulting in a higher concentration of osmium complexes at the hydrophilic heads.[11,34] This may be in part due to interfacial water facilitating the ring-opening reaction. Finally, hydroxyl groups in the phospholipids can also be utilized to form $[OsO_2(OH)_4]^{2-}$.

In the second pathway, Os(VIII) can be reduced via the addition of a reducing agent, in this work, potassium ferrocyanide ($K_4Fe(CN)_6$). $[OsO_4(OH)_2]^{2-}$ is directly reduced outside the lipid bilayer to Os(VI) (Step 4) in parallel with the spontaneous hydroxylation that occurs in Pathway I. This reduction step circumvents the osmate ester formation between the bilayer and greatly accelerates the generation of Os(VI) in the aqueous phase.

Lastly, the formation of OsO_2 occurs via a disproportionation reaction of Os(VI) under biological pH conditions (buffer pH = 7.4).[11,35] Previous X-ray studies of model systems suggested the presence of a dimeric Os(VI) crystal structure with a double oxo bridge.[11,36] Herein, we assume that the same dioxo-bridged osmium species is being formed (Step 5).[28] There are debates regarding the possibility of a tri-osmium product emerging, although this needs future experimental evidence.[28,37] The osmium(VI) dimer is known to be unstable and undergoes asymmetric Os–O bond cleavage. This results in the oxidation of one Os(VI), regenerating Os(VIII), and the reduction of the other Os(VI) center, finally forming $[OsO_2(OH)_2]^{2-}$ in water (Step 6).[38] The dehydroxylation of $[OsO_2(OH)_2]^{2-}$ can readily deposit the lipid-soluble OsO_2 into the bilayer membranes as aggregates (Step 7). The production of OsO_2 contributes to the primary contrast observed in EM images.

Our determination of the source of the contrast in the reduced osmium staining protocol has implications beyond PEEM. Other EM techniques that are commonly used for biological imaging, such as SEM and TEM, adopt the same staining method and will significantly benefit from the proposed contrast mechanism. With the understanding of the speciation of osmium, efforts can be made towards the deposition of a higher concentration of OsO_2 into the lipid membranes. For example, the possibilities to initiate Pathway I in Figure 4 suggest that finding new ways to introduce –OH in proximity to membrane heads could potentially increase the production of $[OsO_4(OH)_2]^{2-}$ for the eventual generation of the contrast relevant OsO_2. Overall, the understanding of the chemical identity of osmium staining promotes intentional modifications for protocol development rather than improvements based upon exhaustive search.

Conclusions

In summary, this work provides a detailed description of the chemical species responsible for obtaining high-contrast images of Os-stained ultra-thin brain slices in electron microscopy. Nanoscale imaging of biological complexes using PEEM enables us to characterize the spatially varying electronic structure of stained UTBS. OsO_2 nanoaggregates are formed in lipid membranes and provide the needed conductivity and contrast due to the metallic electronic structure of OsO_2. We propose a full and detailed scheme of the reactions and pathways necessary for the formation of OsO_2 in the lipid membranes. The determination of the source of contrast, as well as the relevant pathways for OsO_2 generation suggested herein, challenges the long-adopted understanding of Os-staining in biological tissue. Our knowledge of the chemical origin of EM contrast sets the foundation for modifying staining protocols by intentionally engineering the electronic structure of chemical and biological structures on the nanoscale, ultimately achieving sensitive and selective visualization of nanoscale biological components.

Experimental

Sample Preparations

Mouse brain sections were prepared for PEEM imaging following the same protocol used for SEM[4] and for PEEM imaging in our previous work using the "reduced osmium" staining protocol.[12] Briefly, the mouse was perfused transcardially to preserve tissue ultrastructure. The mouse brain was surgically removed and fixed, and a vibratome sectioned brain slice (200–300 μm) was stained with successive rounds of osmium tetroxide and potassium ferrocyanide before ethanol dehydration and embedding with EPON resin. Resin encapsulated brain was then sectioned using an ultramicrotome to a 40–80 nm-thick UTBS which was picked up on a Si substrate with native oxide (*n*-SiO_2/Si) coated with 50 nm of polycrystalline gold. The additional conductive layer was used to prevent sample charging during photoemission.[39] Further details of sample preparation can be found in the Supporting Information.

PEEM Imaging

The UTBS on the Au/n-SiO_2/Si substrate were illuminated using a broadband Hg arc lamp that generates UV continuous-wave (CW) light. The lamp is mounted with a high-pass optical filter allowing photons with energies greater than 4.43 eV (280 nm) to impinge on the sample, and the highest photon energy is approximately 5.0 eV (247 nm) (see full spectrum in Supporting Information Figure S4). The resulting photoelectrons are imaged with a photoemission

electron microscope manufactured by Focus GmbH. The PEEM operates at ultra-high vacuum (base pressure $\approx 5\times10^{-11}$ mbar). Photoexcited electrons are projected, via an electrostatic lens system, onto a double micro-channel plate (MCP), converted to visible light by a phosphor screen, and eventually imaged by a CMOS camera. The typical exposure time for one image is 10 seconds. High-resolution images were obtained by averaging the same regions of interest (ROI) to improve the signal-to-noise ratio. The PEEM is equipped with a high-pass energy filter where only photoelectrons with kinetic energies higher than a given energy threshold can pass and be detected, enabling energy-resolved PEEM images. The energy resolution of the instrument is approximately 50 meV and scans were collected using 100 meV steps.

STEM-EDS and EELS Measurements

Additional characterizations were done using scanning transmission electron microscopy (STEM, JEOL ARM200-CF). The chemical composition of the Os-stained regions were analyzed with energy dispersive spectroscopy (EDS, Oxford XMAX100TLE) to determine the Os : O ratio. A total exposure time of up to 15 minutes was used during EDS measurements due to the thin nature of the specimens. Electron energy-loss spectroscopy (EELS, post-columns Gatan Continuum GIF ER spectrometer) measurements were conducted on osmium-rich regions as well, with an electron probe semi-convergence angle of 17.8 mrad and a collection angle of 53.4 mrad.

Acknowledgements

This work made use of the shared facilities at the University of Chicago Materials Research Science and Engineering Center, supported by the National Science Foundation under award number DMR-2011854. R.L. acknowledges support from the MRSEC Graduate Fellowship (DMR-2011854). A.A. acknowledges support from an Arnold O. Beckman Postdoctoral Fellowship in Chemical Sciences. S.B.K. acknowledges start-up funding support from the University of Chicago and the Neubauer Family Assistant Professors Program. This work was supported in part by funding from the NSF (awards No. 2207383 and No. 2014862). Y.Y. and R.F.K. research was supported by the Army Research Office and was accomplished under grant number W911NF-23-1-0225. The views and conclusions contained in this document are those of the authors and should not be interpreted as representing the official policies, either expressed or implied, of the Army Research Office or the U.S. Government. The U.S. Government is authorized to reproduce and distribute reprints for Government purposes notwithstanding any copyright notation herein. This work made use of instruments in the Electron Microscopy Core at the UIC Research Resources Center. The acquisition of UIC JEOL JEM ARM200CF is supported by an MRI-R^2 grant from the National Science Foundation (DMR-0959470) and the upgraded Gatan Continuum spectrometer was supported by a grant from the NSF (DMR-1626065).

Conflict of Interests

The authors declare no conflict of interest.

Data Availability Statement

The data that support the findings of this study are openly available in Zenodo at https://doi.org/10.5281/zenodo.10125370, reference number 10125370.

Keywords: electron microscopy · biological imaging · osmium characterization · contrast mechanism

[1] V. B. Wigglesworth, *Proc. R. Soc. B: Biol. Sci.* **1957**, *147*, 185.
[2] L. R. Subbaraman, J. Subbaraman, E. J. Behrman, *Inorg. Chem.* **1972**, *11*, 2621.
[3] N. Lalaoui, B. Reuillard, C. Philouze, M. Holzinger, S. Cosnier, A. L. Goff, *Organometallics* **2016**, *35*, 2987.
[4] Y. Hua, P. Laserstein, M. Helmstaedter, *Nat. Commun.* **2015**, *6*, 7923.
[5] K. Song, Z. Feng, M. Helmstaedter, *Nat. Methods* **2023**, *20*, 836.
[6] V. B. Wigglesworth, *Biol. Rev.* **1988**, *63*, 417.
[7] E. L. Scheller, N. Troiano, J. N. Van Houtan, M. A. Bouxsein, J. A. Fretz, Y. Xi, T. Nelson, G. Katz, R. Berry, C. D. Church, C. R. Doucette, M. S. Rodeheffer, O. A. MacDougald, C. J. Rosen, M. C. Horowitz, *Methods Enzymol.* **2014**, *537*, 123.
[8] L. Graham, J. M. Orenstein, *Nat. Protoc.* **2007**, *2*, 2439.
[9] A. M. Seligman, H. L. Wasserkrug, J. S. Hanker, *J. Cell Biol.* **1966**, *30*, 424.
[10] K. P. C. Vollhardt, N. E. Schore, Organic Chemistry: Structure and Function, W. H. Freeman, New York, 6th edition **2011**.
[11] D. L. White, S. Andrews, J. Faller, R. J. Barrnett, *Biochim. Biophys. Acta – Biomembr.* **1976**, *436*, 577.
[12] K. M. Boergens, G. Wildenberg, R. Li, L. Lambert, A. Moradi, G. Stam, R. Tromp, S. J. van der Molen, S. B. King, N. Kasthuri, Photoemission electron microscopy for connectomics **2023**, preprint at https://www.biorxiv.org/content/early/2023/09/06/2023.09.05.556423.1.
[13] T. Tsutsumi, T. Miyamoto, H. Niimi, Y. Kitajima, Y. Sakai, M. Kato, T. Naito, K. Asakura, *Solid State Electron.* **2007**, *51*, 1360.
[14] P. U. Gilbert, *J. Electron Spectros. Relat. Phenomena* **2012**, *185*, 395.
[15] C. A. Schmidt, E. Tambutté, A. A. Venn, Z. Zou, C. C. Alvarez, L. S. Devriendt, H. A. Bechtel, C. A. Stifler, S. Anglemyer, C. P. Breit, C. L. Foust, A. Hopanchuk, C. N. Klaus, I. J. Kohler, I. M. LeCloux, J. Mezera, M. R. Patton, A. Purisch, V. Quach, J. S. Sengkhammee, T. Sristy, S. Vattem, E. J. Walch, M. Albéric, Y. Politi, P. Fratzl, S. Tambutté, P. U. Gilbert, *Nat. Commun.* **2024**, *15*, 1812.
[16] A. Skallberg, K. Bunnfors, C. Brommesson, K. Uvdal, *Anal. Chem.* **2019**, *91*, 13514.
[17] A. Skallberg, K. Bunnfors, C. Brommesson, K. Uvdal, *Nano Lett.* **2020**, *21*, 222.
[18] N. Kasthuri, K. J. Hayworth, D. R. Berger, R. L. Schalek, J. A. Conchello, S. Knowles-Barley, D. Lee, A. Vázquez-Reina, V. Kaynig, T. R. Jones, M. Roberts, J. L. Morgan, J. C. Tapia, H. S. Seung, W. G. Roncal, J. T. Vogelstein, R. Burns, D. L. Sussman, C. E. Priebe, H. Pfister, J. W. Lichtman, *Cell* **2015**, *162*, 648.
[19] F. Reinert, S. Hüfner, *New J. Phys.* **2005**, *7*, 97.
[20] S. Hüfner, S. Schmidt, F. Reinert, *Nucl. Instrum. Methods Phys. Res. A: Accel. Spectrom. Detect. Assoc. Equip.* **2005**, *547*, 8.
[21] M. F. Pignataro, M. G. Herrera, V. I. Dodero, *Molecules* **2020**, *25*, 4854.
[22] D. M. Close, *J. Phys. Chem. A* **2011**, *115*, 2900.
[23] V. Pershina, T. Bastug, B. Fricke, S. Varga, *J. Chem. Phys.* **2001**, *115*, 792.
[24] J. C. Green, N. Kaltsoyannis, K. H. Sze, M. A. Mac-Donald, *Chem. Phys. Lett.* **1990**, *175*, 359.
[25] A. Regoutz, A. M. Ganose, L. Blumenthal, C. Schlueter, T.-L. Lee, G. Kieslich, A. K. Cheetham, G. Kerherve, Y.-S. Huang, R.-S. Chen, G. Vinai, T. Pincelli, G. Panaccione, K. H. L. Zhang, R. G. Egdell, J. Lischner, D. O. Scanlon, D. J. Payne, *Phys. Rev. Mater.* **2019**, *3*, 025001.
[26] D. B. Rogers, S. R. Butler, R. D. Shannon, A. Wold, R. Kershaw, *Inorg. Synth.* **2016**, pages 135–145.
[27] Y. Hayakawa, S. Kohiki, M. Arai, H. Yoshikawa, S. Fukushima, K. Wagatsuma, M. Oku, F. Shoji, *Phys. Rev. B* **1999**, *59*, 11125.

[28] D. Belazi, S. Solé-Domènech, B. Johansson, M. Schalling, P. Sjövall, *Histochem. Cell Biol.* **2009**, *132*, 105.
[29] M. Schroeder, *Chem. Rev.* **1980**, *80*, 187.
[30] Y. Ogino, H. Chen, H.-L. Kwong, K. B. Sharpless, *Tetrahedron Lett.* **1991**, *32*, 3965.
[31] H. C. Kolb, M. S. VanNieuwenhze, K. B. Sharpless, *Chem. Rev.* **1994**, *94*, 2483.
[32] A. A. Khan, J. C. Riemersma, H. L. Bbooij, *J. Histochem. Cytochem.* **1961**, *9*, 560.
[33] J. D. Nickels, J. Katsaras, *Subcell. Biochem.* **2015**, *71*, 45.
[34] W. Stoeckenius, *Protoplasma* **1967**, *63*, 214.
[35] J. F. Cairns, H. L. Roberts, *J. Chem. Soc. C* **1968**, *0*, 640.
[36] B. A. Cartwright, W. P. Griffith, M. Schröder, A. C. Skapski, *J. Chem. Soc.* **1978**, *0*, 853.
[37] S. Ströh, E. W. Hammerschmith, D. W. Tank, H. S. Seung, A. A. Wanner, *eLife* **2022**, *11*, e72147.
[38] E. D. Korn, *J. Cell Biol.* **1967**, *34*, 627.
[39] G. B. Birrell, K. K. Hedberg, D. L. Habliston, O. Griffith, *Ultramicroscopy* **1991**, *36*, 235.

Manuscript received: April 19, 2024
Accepted manuscript online: July 22, 2024
Version of record online: September 12, 2024